Percolative Scale-Free Behavior in the Boiling Crisis

Limiao Zhang, Jee Hyun Seong, and Matteo Bucci*
Department of Nuclear Science and Engineering, Massachusetts Institute of Technology, Cambridge, Massachusetts 02139, USA

(Received 26 September 2018; published 5 April 2019)

We present the first experimental observations of scale-free behavior in the bubble footprint distribution during the boiling crisis of water, in pool and flow boiling conditions. We formulate a continuum percolation model that elucidates how the scale-free behavior emerges from the near-wall stochastic interaction of bubbles and provides a criterion to predict the boiling crisis. It also offers useful insights on how to engineer surfaces that enhance the critical heat flux limit.

DOI: 10.1103/PhysRevLett.122.134501

Boiling is a very efficient heat transfer process, widely applied for heat management, e.g., in electric power stations and high-power-density electronic devices. In such systems, the boiling process dynamics is driven by the heat flux transferred from the heated surface. An increase in the heat flux produces a rise of the surface temperature, which in turn increases the bubble nucleation site density and departure frequency. The chief vulnerability of boiling is an instability known as the boiling crisis, triggered when the heat flux reaches the critical heat flux (CHF) limit. This phenomenon coincides with a sudden transition from a nucleate boiling regime, with discrete bubbles on the surface, to a film boiling regime, where a stable vapor layer blankets the entire heating surface [1]. Such a layer causes a drastic degradation of the heat removal process, resulting in a potentially catastrophic escalation of the heater temperature. Thus, understanding the boiling crisis, and predicting and possibly enhancing the CHF are desirable goals for the safety and economics of many thermal systems.

Experimental investigations have revealed that CHF depends on fluid properties and operating conditions, heater geometry, surface material, orientation, and properties (e.g., roughness, porosity, and intrinsic wettability). Many mechanisms and models have been proposed to capture these effects [2]. However, there is still no agreement within the thermal science community on the actual trigger mechanism for the boiling crisis, let alone a universal model to predict it. Historically, most models have been built assuming that the boiling crisis is triggered by a macroscale hydrodynamic instability in the countercurrent vapor-liquid flow far from the heating surface [3,4]. More recently, several authors have argued that the boiling crisis is instead a near-wall phenomenon, determined by microscale fluid-solid interactions on the heating surface [5–9]. However, while most models attempt to capture the CHF limits leveraging scale-based descriptions of presumed trigger mechanisms, recent findings suggest that the boiling crisis is a scale-free, critical phenomenon. This perception stems from observations of power-law spectra in the temperature fluctuations of wire heaters [10], energy distributions of acoustic emissions during surface quenching with liquid nitrogen [11], and bubble size distributions in slowed-down boiling of hydrogen at reduced gravity [12]. The predictions of a numerical lattice spin model presented in Ref. [11] suggest that the critical behavior may be the result of a bubble percolation process. The observations in Ref. [12] seem to corroborate this hypothesis. However, one cannot exclude that these findings are affected by the special dynamics of the boiling process in their operating conditions (e.g., the bubble departure diameter tends to infinity) [12]. To affirm the percolative scale-free nature of the boiling crisis, an experimental and theoretical demonstration in conditions of broad relevance, such as the pool and flow boiling of water, is still unavailable and clearly necessary.

In this Letter, we present the first experimental study of bubble footprint distributions during the pool and flow boiling of water. At CHF, the experimental distributions follow a power law $1/A^{\gamma}$ with a critical exponent γ smaller than 3, which demonstrates the scale-free nature of the boiling crisis [13]. Our experiment also enables the measurement of fundamental boiling parameters (i.e., nucleation site density, growth time, bubble departure frequency, and radius), and is instrumental in revealing the dynamics of the bubble interaction process. Inspired by these observations, we develop a bubble percolation model based on the continuum percolation theory [14]. The model explains and captures how the scale-free behavior at the boiling crisis emerges from the near-wall stochastic interaction of individual bubbles. It also provides a criterion to predict the boiling crisis.

We run boiling experiments featuring specially designed heaters (see schematic in Fig. 1) consisting of a 1 mm thick, infrared (IR) transparent sapphire substrate coated on one side with an electrically conductive, IR opaque, 0.7 μm thick layer of indium-doped tin oxide (ITO). The thin ITO coating, in contact with water, is the Joule heating element. It has negligible thermal resistance and heat capacity;

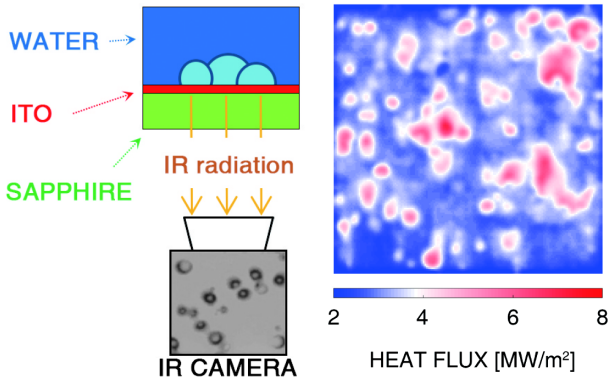

FIG. 1. The schematic on the left shows the ITO-sapphire heater configuration with the IR diagnostics (not to scale). The image on the right shows a typical instantaneous heat flux distribution on the boiling surface (1×1 cm^2, flow boiling test at atmospheric pressure, bulk temperature 95 °C, mass flux 2000 kg/m^2/s, and heat flux 3460 kW/m^2).

i.e., the ITO temperature coincides with the actual temperature on the boiling surface. The heater is installed in a pool boiling or a flow boiling apparatus, as detailed in the Supplemental Material, Sec. 1 [15]. During the experiments, we increase the heat flux released by the ITO in a sequence of steady steps, up to the critical heat flux that causes the boiling crisis. For each heat flux, the infrared radiation emitted by the ITO and transmitted through sapphire is recorded by a high-speed infrared camera (with a temporal resolution of 400 μs and a spatial resolution of 115 μm/pixel) and postprocessed to obtain the time-dependent temperature and heat flux distributions on the boiling surface [16]. The high temporal and spatial resolution enabled by this technique is key to capturing the dynamics of the boiling process up to the boiling crisis. Bubbles nucleate, grow, perhaps coalesce, and depart from the surface. The life of discrete bubbles is described through finite, characteristic parameters, i.e., departure frequency, growth time, and departure diameter. Bubble interaction is instead a stochastic process determined by these parameters, as well as the distance among the nucleation sites, i.e., the nucleation site density. A typical output is shown in Fig. 1, where we can clearly distinguish the patches of individual and coalesced bubbles attached to the surface.

These distributions are processed to measure nucleation site density, bubble wait time and growth time and, importantly, the footprint area of each bubble on the boiling surface, using the techniques described in Ref. [17]. The measured bubble footprint area probability density functions (PDFs) for saturated pool boiling and subcooled flow boiling tests run at atmospheric pressure are shown in Figs. 2(a) and 2(c) (for the flow boiling tests the bulk temperature is 95 °C, i.e., ~5 °C below the saturation temperature at the system pressure, the mass flux is 2000 kg/m^2/s). For low heat fluxes (e.g., at 300 kW/m^2 and 1270 kW/m^2 for the pool boiling and flow boiling experiments, respectively), most of

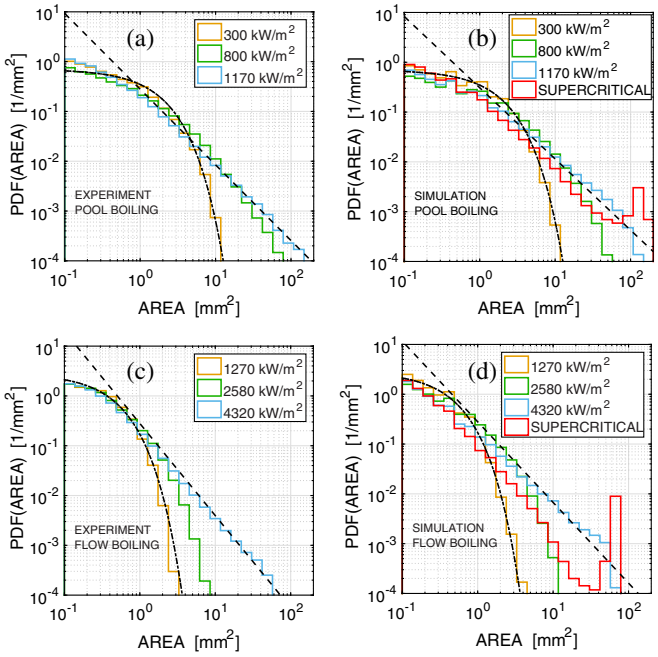

FIG. 2. (a) Experimental and (b) simulated bubble footprint area PDFs at different heat fluxes, from nucleate boiling (orange, 300 kW/m^2) till the boiling crisis (sky blue, 1170 kW/m^2) for the saturated pool boiling tests at atmospheric pressure. The dash-dotted line represents Eq. (1) obtained with an average bubble radius $\langle R \rangle = 0.6$ mm. The dashed line represents a power-law distribution $1/A^{\gamma}$. The power-law exponents are $\gamma = 1.52 \pm 0.01$ and $\gamma = 1.43 \pm 0.01$ for the experimental and the simulated PDFs, respectively. The red curve in (b) corresponds to a supercritical case which represents the film boiling regime. (c) and (d) are analogous experimental and simulated results for the subcooled flow boiling test. Here, the average bubble radius for the exponential fitting, i.e., Eq. (1), is $\langle R \rangle = 0.3$ mm. The power-law critical exponents are $\gamma = 1.85 \pm 0.01$ and $\gamma = 1.62 \pm 0.01$ for the experimental and the simulated PDFs, respectively.

the bubbles are isolated; i.e., they seldom interact with each other. We observe that, under these conditions, the footprint area PDF is exponentially damped (as also observed in Ref. [12]), and can be fitted by

$$P(A) = ce^{-cA}. \tag{1}$$

Assuming that the footprint of individual bubbles is circular, the bubble footprint radius PDF is

$$P(R) = 2\pi Rce^{-c\pi R^2}. \tag{2}$$

Note that from Eq. (2), c is related to the average bubble footprint radius $\langle R \rangle (= 1/\sqrt{4c})$. As the heat flux increases (e.g., at 800 and 2580 kW/m^2 for the pool boiling and flow boiling experiments, respectively), bubbles merge more and more frequently, and large bubble patches start to appear on the boiling surface. When the boiling crisis

occurs (at 1170 kW/m^2 and 4320 kW/m^2 for the pool boiling and flow boiling experiments, respectively), the bubble footprint area PDF is a power-law function $1/A^{\gamma}$. In pool boiling [Fig. 2(a)], the critical exponent γ evaluated by the maximum likelihood method and tested by the Kolmogorov-Smirnoff method [18,19] is 1.52 ± 0.01. The critical exponent for the flow boiling test [Fig. 2(c)] is instead 1.85 ± 0.01.

The emergence of scale-free behavior at CHF indicates the absence of a characteristic scale in the boiling crisis, also in the pool and flow boiling of water. The different values of γ suggest that the critical exponent depends on the operating conditions, which seems reasonable given the different boiling phenomenology (e.g., different forces affecting bubble departure dynamics) in pool boiling and flow boiling.

Inspired by our experimental observations, we introduce a Monte Carlo (MC) model based on the continuum percolation theory [14], which captures the footprint area PDFs. From our experiments, we know the nucleation site density N'', the bubble growth time t_g, and the bubble departure frequency f for each heat flux. Given a surface of area A equal to our heater active area (i.e., 1×1 cm^2), we randomly generate $N''A$ nucleation sites. The probability to have a bubble growing out of a certain nucleation site is equal to $t_g f$. Thus, given a random number $b \in [0, 1]$, if $b \leq t_g f$, we generate a bubble, otherwise, we move to the next nucleation site. Similarly, if a nucleation site is already covered by a bubble growing out of another nucleation site, we move to the next one. When generating a bubble, its radius is determined according to the distribution of individual bubbles, Eq. (2), measured experimentally (for the derivation details see the Supplemental Material, Sec. 2 [15]):

$$R = \sqrt{-\frac{4\langle R\rangle^2}{\pi}\ln(1-q)}, \tag{3}$$

where $q \in [0, 1]$ is a random number. The average bubble radius $\langle R\rangle$ is the last characteristic quantity obtained from the experiments. However, the average size of individual bubbles can only be accurately measured at low heat fluxes, i.e., when bubbles do not interact with each other. At high heat fluxes, the individual bubble footprint area PDF shrinks compared to the distribution that bubbles would have if they were growing without ever interacting. To overcome this limitation, the value of $\langle R\rangle$ at high heat flux is estimated scaling the value of $\langle R\rangle$ at low heat fluxes by a bubble departure, force balance model [20] (for the derivation details and a complete description of the experimental data used as input in the MC model, see the Supplemental Material, Sec. 2 [15]). We repeat this procedure throughout the nucleation sites. A typical output image from one cycle is shown in Fig. 3, where we sample the areas of the bubble patches, for both individual and coalesced bubbles. Then, the process is repeated many times, until we obtain a converged bubble footprint area PDF.

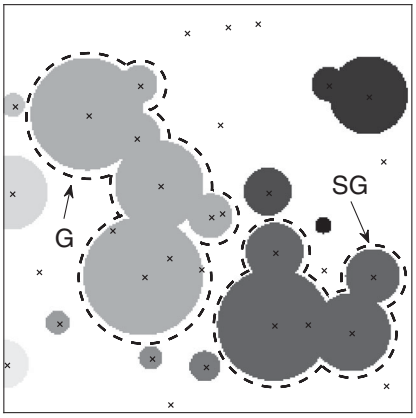

FIG. 3. Typical output of a MC iteration, with the identification of the giant G and the second giant SG clusters. Bubble footprints of the same color belong to the same cluster. Small crosses indicate nucleation sites.

The predicted PDFs are shown in Figs. 2(b) and 2(d). The MC model captures the trends of the experimental PDFs correctly, at any heat flux level. The PDF at CHF follows a power law, which corroborates the thesis of the boiling crisis as a percolative near-wall phenomenon. Note that, despite the simplicity of the model, the simulated critical exponents are similar to the ones measured experimentally.

The scale-free behavior is typical in critical phenomena [21], including percolative processes, such as forest fires [22] or traffic jams [23]. Percolation is a powerful tool to analyze phase transition in stochastic processes, with multiple applications in natural and engineering sciences [24]. Here, we show how continuum percolation can be used to predict the boiling crisis, assuming that we know how nucleation site density, bubble growth time and departure frequency, and bubble radius change with the heat flux, i.e., the boiling driving force. In classic site percolation models, a site on a lattice is occupied with probability p. Two neighbor nodes are connected if they are both occupied. A cluster is defined as a group of sites connected by near-neighbor distances [25]. There is a percolation threshold p_c below which only a few isolated clusters exist, and the size of these clusters increases with p. Conversely, for p above p_c, a single, large cluster percolates through the lattice. The emergence of a spanning cluster indicates the occurrence of percolation transition. The percolation threshold p_c coincides with a maximum of the second largest cluster size, which provides the system failure criterion, and a scale-free cluster size distribution [26]. In continuum percolation, instead, the discrete lattice sites are replaced by penetrable objects (e.g., bubble footprints) in a continuous space (e.g., the boiling surface).

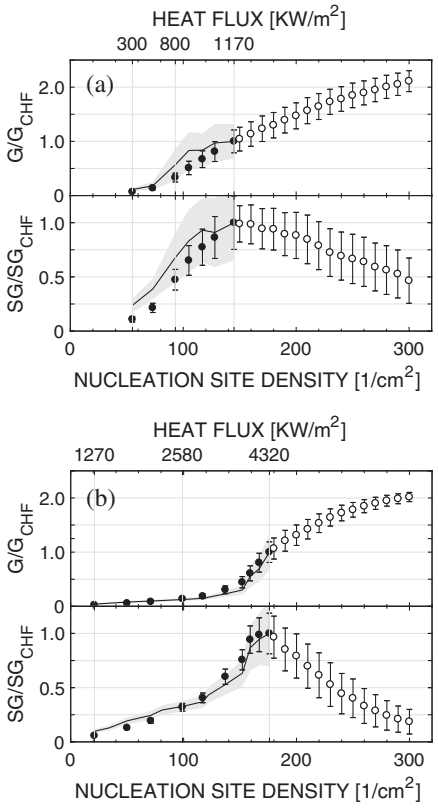

FIG. 4. Measured (solid line) and simulated (filled or empty dots) trends of the G and SG area as a function of the nucleation site density in pool boiling (a) and flow boiling conditions (b).

The percolation threshold is given by a critical filling factor η_c, which plays a role similar to p_c in site percolation [27].

In our work, we sample the area of the giant G and the second giant SG cluster (see Fig. 3), i.e., the bubble patches with the largest and second largest footprint area, respectively. The trends of the G and SG area, both measured (solid line) and simulated (filled dots), are plotted in Fig. 4 as a function of the nucleation site density, which monotonically increases with the heat flux. When the nucleation site density is small, for low heat fluxes, bubbles do not coalesce and the sizes of the G and SG clusters are very close, and are consistent with the size of individual bubbles.

Then, as the heat flux increases, the growth of the clusters is first determined by the attachment of discrete bubbles. However, as the clusters grow bigger (i.e., for higher and higher heat fluxes), they start to coalesce with each other, and the larger is a cluster, the higher is the probability of absorbing smaller ones. Thus, the G and SG areas increase with the nucleation site density up to the N'' corresponding to the boiling crisis (i.e., 145 sites/cm^2 for saturated pool boiling test and 176 sites/cm^2 for the flow boiling test). Right before the CHF, the G area is still increasing, while the SG area seems to reach a maximum. Note that, as the boiling crisis is detected, experiments are promptly interrupted to avoid the burnout of our heating element. Thus, the "experiment" is continued numerically by adding extra nucleation sites to the simulations. The results (hollow dots in Fig. 4) confirm that the boiling crisis coincides with a maximum of the SG cluster area. It indicates a critical point, beyond which the process becomes unstable, as the largest cluster G rapidly absorbs all the other clusters; i.e., there is a rapidly growing vapor layer, covering the entire boiling surface. The red curves in Figs. 2(b) and 2(d) correspond to the simulated bubble footprint area PDFs in supercritical conditions ($N'' = 300$ sites/cm^2 for both pool boiling and flow boiling conditions), showing the emergence of a large spanning vapor patch. Note that the maximum in the SG size coincides with the occurrence of a power-law distribution, as expected in percolation criticality [26]. It provides a criterion to predict the boiling crisis and, considering the analogy with the dynamics of other percolative processes [26], further demonstrates the percolative, critical nature of the boiling crisis.

In conclusion, our investigation of pool and flow boiling of water (i.e., conditions of broad interest) reveals that the boiling crisis is a percolative, scale-free phenomenon. We propose a MC model based on continuum percolation that describes the near-wall stochastic interaction of bubbles. The model captures how the bubble footprint area distribution evolves with the heat flux (i.e., the process driving force), through a change of nucleation site density N'', bubble growth time and departure frequency $t_g f$, and bubble radius $\langle R \rangle$, i.e., the model inputs. The model provides a criterion to predict the boiling crisis. The growth of a spanning vapor patch, i.e., the boiling crisis, coincides with a critical point in the percolation process, defined by the "critical triplet" N'', $t_g f$, $\langle R \rangle$ that maximizes the SG area. This finding has practical implications. The change of nucleation site density, bubble growth time, departure frequency, and bubble radius with heat flux is determined by surface properties and features, e.g., wettability and morphology. Thus, the model can be used to assess the performance of different surfaces and identify surface engineering solutions for which "critical triplets" occur at higher CHF values.

We thank J. Buongiorno, E. Baglietto, S. Yip, G. Su, and A. Kossolapov for many insightful comments. L. Z. acknowledges the Chinese Scholarship Council (CSC, 201706020179). J. H. S. acknowledges the funding support from the Consortium for Advanced Simulations of Light Water Reactors [28], under U.S. Department of Energy Contract No. DE-AC05-00OR22725.

*mbucci@mit.edu

[1] J. G. Collier and J. R. Thome, *Convective Boiling and Condensation* (Oxford University Press, New York, 1994); V. P. Carey, *Liquid-Vapor Phase Change Phenomena: An*

Introduction to the Thermophysics of Vaporization and Condensation Processes in Heat Transfer Equipment (Taylor and Francis, New York, 2008).
[2] G. Liang and I. Mudawar, Int. J. Heat Mass Transfer **117**, 1352 (2018).
[3] N. Zuber, Trans. ASME **80**, 711 (1958).
[4] S. G. Kandlikar, J. Heat Transfer **123**, 1071 (2001).
[5] K. Sefiane, D. Benielli, and A. Steinchen, Colloids Surf. A **142**, 361 (1998).
[6] T. Theofanous, J. Tu, A. Dinh, and T.-N. Dinh, Exp. Therm. Fluid. Sci. **26**, 775 (2002); T. Theofanous, T.-N. Dinh, J. Tu, and A. Dinh, Exp. Therm. Fluid. Sci. **26**, 793 (2002).
[7] V. Yagov, Therm. Eng. **35**, 65 (1988).
[8] V. Nikolayev, D. Chatain, Y. Garrabos, and D. Beysens, Phys. Rev. Lett. **97**, 184503 (2006).
[9] J. Jung, S. J. Kim, and J. Kim, J. Heat Transfer **136**, 041501 (2014).
[10] V. N. Skokov, V. P. Koverda, A. V. Reshetnikov, V. P. Skripov, N. A. Mazheiko, and A. V. Vinogradov, Int. J. Heat Mass Transfer **46**, 1879 (2003).
[11] P. Lloveras, F. Salvatpujol, L. Truskinovsky, and E. Vives, Phys. Rev. Lett. **108**, 215701 (2012).
[12] T. Charignon, P. Lloveras, D. Chatain, L. Truskinovsky, E. Vives, D. Beysens, and V. S. Nikolayev, Phys. Rev. E **91**, 053007 (2015).
[13] A. L. Barabási, *Networks Science* (Cambridge University Press, Cambridge, England, 2016); R. Cohen and S. Havlin, *Complex Networks* (Cambridge University Press, Cambridge, England, 2010).
[14] E. N. Gilbert, J. Soc. Ind. Appl. Math. **9**, 533 (1961).
[15] See Supplemental Material at http://link.aps.org/supplemental/10.1103/PhysRevLett.122.134501 for details about the experimental apparatus (Sec. 1) and a complete description of the experimental data used as input in the MC model (Sec. 2).
[16] M. Bucci, A. Richenderfer, G.-Y. Su, T. McKrell, and J. Buongiorno, Int. J. Multiphase Flow **83**, 115 (2016).
[17] A. Richenderfer, A. Kossolapov, J. H. Seong, G. Saccone, E. Demarly, R. Kommajosyula, E. Baglietto, J. Buongiorno, and M. Bucci, Exp. Therm. Fluid. Sci. **99**, 35 (2018).
[18] A. Clauset, C. R. Shalizi, and M. E. Newman, SIAM Rev. **51**, 661 (2009).
[19] M. Newman, Contemp. Phys. **46**, 323 (2005).
[20] T. Mazzocco, W. Ambrosini, R. Kommajosyula, and E. Baglietto, Int. J. Heat Mass Transfer **117**, 119 (2018).
[21] H. E. Stanley, *Phase Transitions and Critical Phenomena* (Clarendon Press, Oxford, 1971).
[22] D. L. Turcotte, Rep. Prog. Phys. **62**, 1377 (1999).
[23] L. Zhang, G. Zeng, D. Li, H.-J. Huang, H. E. Stanley, and S. Havlin, arXiv:1804.11047.
[24] A. Herega, J. Mater. Sci. Eng. **5**, 409 (2015).
[25] D. Stauffer, Phys. Rep. **54**, 1 (1979).
[26] A. Bunde and S. Havlin, *Fractals and Disordered Systems* (Springer-Verlag, Berlin Heidelberg, 1996).
[27] S. Mertens and C. Moore, Phys. Rev. E **86**, 061109 (2012).
[28] http://www.casl.org.